



Graphene composites with Ru-RuO₂ heterostructures: Highly efficient Mott–Schottky-type electrocatalysts for pH-universal water splitting and flexible zinc–air batteries

Nan Wang ^{a,1}, Shunlian Ning ^{c,1}, Xiaolong Yu ^b, Di Chen ^a, Zilong Li ^a, Jinchang Xu ^a, Hui Meng ^{a,*}, Dengke Zhao ^c, Ligui Li ^{c,*}, Qiming Liu ^d, Bingzhang Lu ^d, Shaowei Chen ^{d,*}

^a Guangdong Provincial Key Laboratory of Optical Fiber Sensing and Communications, Siyuan Laboratory, Guangzhou Key Laboratory of Vacuum Coating Technologies and New Energy Materials, Guangdong Provincial Engineering Technology Research Center of Vacuum Coating Technologies and New Energy Materials, Department of Physics, Jinan University, Guangzhou, Guangdong 510632, China

^b Guangdong Provincial Key Laboratory of Petrochemical Pollution Processes and Control, School of Environmental Science and Engineering, Guangdong University of Petrochemical Technology, Maoming, Guangdong 525000, China

^c New Energy Research Institute, College of Environment and Energy, South China University of Technology, Guangzhou 510006, China

^d Department of Chemistry and Biochemistry, University of California, 1156 High Street, Santa Cruz, CA 95064, United States

ARTICLE INFO

Keywords:

Mott–Schottky junction
Graphene nanocomposite
Ru–RuO₂ heterostructure
Water splitting
Metal–air battery

ABSTRACT

Development of high-efficiency electrocatalysts for pH-universal overall water splitting is a critical step towards a sustainable hydrogen economy. Herein, graphene nanocomposites with Ru–RuO₂ Mott–Schottky heterojunctions (Ru–RuO₂@NPC) are prepared pyrolytically and exhibit a remarkable electrocatalytic activity at pH = 0–14 towards both oxygen/hydrogen evolution reactions and overall water splitting, as compared to commercial RuO₂ and Pt/C. Ru–RuO₂@NPC can also be used as an effective air cathode catalyst for flexible, rechargeable zinc–air batteries. Density functional theory calculations show that the formation of Ru–RuO₂ heterojunctions moderately enhances the surface charge density of metallic Ru and brings the d states closer to Fermi level, as compared to that of RuO₂ alone, leading to improved intrinsic electrocatalytic activity towards these important reactions. These results demonstrate the significance of Mott–Schottky heterojunctions in the development of high-efficiency electrocatalysts for various new energy technologies.

1. Introduction

Electrochemical water splitting to produce H₂ and O₂ represents a promising technology to mitigate the aggravated energy crisis and environmental problems arising from the combustion of fossil fuels, as hydrogen possesses a high gravimetric energy density (142 MJ kg⁻¹) and is an ideal alternative energy source [1–3]. In such water electrolysis, effective catalysts are needed for both the hydrogen evolution reaction (HER) at the cathode and oxygen evolution reaction (OER) at the anode, so as to achieve a high current density in actual use [4,5]. This is particularly challenging for OER, primarily due to the complex reaction pathways and sluggish electron-transfer kinetics [6]. Early studies have been mostly focused on catalysts for either the HER or OER half reaction in a particular solution medium (i.e., acidic or alkaline), whereas

pH-universal, bifunctional catalysts have remained scarce [7–9]. Therefore, development of high-performance catalysts that are active for both HER and OER in a wide range of pH is of fundamental significance in the practical implementation of such technologies [10,11]. Currently, platinum (Pt) and iridium (Ir) based nanoparticles are the benchmark electrocatalysts for HER and OER, respectively [12,13]. However, the low natural reserves and high costs of these noble metals significantly limit their wide-spread applications [14]. In recent years, earth-abundant transition metals have attracted extensive attention; yet their activity and durability have remained subpar, as compared to the commercial benchmarks [15]. Within this context, less expensive noble metals, such as Ru, have been recognized as promising electrocatalysts, due largely to the competitive prices (e.g., ca. \$40 per ounce for Ru, as compared to ca. \$1000 for Pt and \$500 for Ir) and electrocatalytic

* Corresponding authors.

E-mail addresses: tmh@jnu.edu.cn (H. Meng), esguili@scut.edu.cn (L. Li), shaowei@ucsc.edu (S. Chen).

¹ These authors contributed equally to this work.

performances. This is mainly driven by the similar electronic energy structures of Ru and RuO₂ to those of Pt and IrO₂ [16,17].

Nevertheless, several issues are difficult to ignore. For example, metallic Ru has shown good catalytic activity towards HER, but limited towards OER, while RuO₂ is far more active towards OER but not so much for HER [18,19]. Therefore, an immediate question arises. Can a Ru-RuO₂ heterostructure serve as effective bifunctional catalysts towards both HER and OER?

Notably, surface and interfacial engineering has been demonstrated as an effective strategy to manipulate the electrochemical performance of metal catalysts, and formation of metal-semiconductor Mott-Schottky (M-S) heterojunctions represents a unique strategy [20]. This is mainly due to electron transfer that occurs spontaneously at the heterojunction interface, and the resulting charge redistribution is conducive to the electron-transfer reactions at the electrode surface [20]. Mechanistically, the built-in electric field promotes local charge polarization in the heterojunction interface, and greatly improves the adsorption of the critical reaction intermediates, leading to enhanced electrocatalytic activity [21]. For instance, Li et al. [22] prepared Co/CoP M-S nanoparticles as efficient catalysts for both HER and OER. In another study [23], Ding et al. demonstrated the significance of enhanced electron transfer and mass transport of a jellyfish-like M-S nanostructure in catalyzing oxygen reduction reaction (ORR), where spontaneous electron transfer from Fe to N-doped carbon at the heterojunction interface was found to boost the electron-transfer reaction on the electrode surface. Liu et al. proposed a self-gating mechanism to account for the electronic conduction modulation of semiconductors during electrocatalysis, and argued that the type of semiconductor catalyst (i.e., n or p type) is closely related to the electrocatalytic activity towards specific reactions [24]. However, the intrinsic mechanism of the electrocatalytic activity of these M-S heterojunctions has remained largely unexplored, although the activity has been known to be correlated to the electron density and d-band structure of the active centers [20,21].

In the present study, motivated by results from density functional theory (DFT) calculations, functional nanocomposites were prepared via direct thermal annealing of N,P-codoped reduced graphene oxide nanosheets with ruthenium(III) chloride (RuCl₃) and thiourea (CH₄N₂S), where Ru-RuO₂ M-S nanoparticles were deposited on the nanosheet surface. The resulting Ru-RuO₂@NPC nanocomposites exhibited excellent electrocatalytic activity towards both HER and OER within a wide range of pH and could serve as effective bifunctional catalysts for overall water splitting and as reversible oxygen catalysts for flexible zinc-air battery. This was largely ascribed to charge transfer at the Ru-RuO₂ M-S heterojunctions, such that the d-band center (E_d) at the interface fell in the intermediate between those of Ru and RuO₂, an optimal condition for the adsorption and desorption of key reaction intermediates (e.g., *H, *O, *OH, and *OOH).

2. Experimental section

2.1. Synthesis of Ru-RuO₂@NPC nanocomposites

Experimentally, graphene oxide nanosheets were first synthesized by following a literature procedure [25]. Two separate solutions were then prepared, one with 0.123 mmol of phytic acid dispersed into 10 mL of deionized water, and the other with 0.123 mmol of RuCl₃·H₂O dissolved also in 10 mL of deionized water. These two solutions were mixed under vigorous stirring, into which was added 90 mg of the graphene oxide dispersion in 20 mL of deionized water and 1 g of dicyandiamide. The solution pH was adjusted to neutral with sodium bicarbonate. The resulting solution was then loaded into a 50 mL Teflon-lined stainless-steel autoclave, which was sealed and heated at 150 °C for 6 h. The obtained gel-like product was collected and thermally treated in a tube furnace at 800 °C for 2 h under an Ar atmosphere. The resulting sample was denoted as Ru-RuO₂@NPC.

Three control samples were also prepared in the same manner with

different modifications. RuO₂@NPC was obtained with the precursor solution pH increased to 9, Ru@NPC was synthesized at a lower pH of 5 with thermal annealing conducted in a mixed atmosphere of Ar (90%) and H₂ (10%), and NPC was produced without the addition of RuCl₃.

2.2. Characterization

Transmission electron microscopy (TEM) measurements were conducted on a Tecnai G2-F20 microscope equipped with an EDS detector at an acceleration voltage of 100 kV. Scanning electron microscopy (SEM) measurements were conducted with a field-emission scanning electron microscope (S-4800, Hitachi). X-ray absorption spectroscopy (XAS) measurements were performed in the Shanghai Synchrotron Radiation Facility in the fluorescence mode at room temperature (298 K). X-ray photoelectron spectroscopy (XPS) measurements were performed on a Phi X-tool instrument. X-ray diffraction (XRD) patterns were recorded with a Bruker D8-Advance diffractometer using Cu K_α radiation. Nitrogen adsorption/desorption isotherms were acquired at 77 K using a Micromeritics ASAP 2010 instrument. Raman spectroscopic studies were conducted with a Renishaw inVia instrument. Inductively coupled plasma optical emission spectrometry (ICP-OES) analysis was performed with a SPECTROBLUE SOP instrument. Hydrogen-temperature programmed desorption (H₂-TPR) experiments were carried out in a quartz microreactor using 50 mg of the sample with an AutoChem II 2920 instrument at the heating rate of 10 K min⁻¹ in a 10% H₂/Ar mixture (30 mL min⁻¹) from room temperature to 1023 K.

2.3. Electrochemistry

All electrochemical tests were performed under ambient conditions. OER, HER and ORR tests were conducted in a three-electrode set-up, and overall water splitting was performed in a two-electrode system with a CHI 750E electrochemical workstation in different aqueous solutions (1.0 M KOH, 0.5 M H₂SO₄, 0.01 M phosphate buffer solution (PBS), and 0.1 M KOH). A rotating ring-disk electrode (RRDE) with a glassy carbon disk and gold ring was used as the working electrode. A Ag/AgCl electrode (3 M KCl) and a carbon rod were used as the reference and counter electrode, respectively.

To prepare the working electrode, 4 mg of the catalysts prepared above was dispersed in 1 mL of a 5% Nafion solution in ethanol under sonication for 0.5 h. Then, 20 μL of the catalyst ink was dropcast onto the surface of the glassy carbon electrode (GCE) at a catalyst loading of 0.408 mg cm⁻². OER and HER measurements were carried out in 0.5 M H₂SO₄, 1.0 M KOH and 0.01 M PBS aqueous solutions. In electrochemical measurements, the Ag/AgCl reference electrode was calibrated with respect to a reversible hydrogen electrode (RHE), and all potentials reported in the present study were referenced to this RHE.

2.4. Fabrication of zinc-air batteries

To assemble liquid-phase Zn–air batteries, a piece of carbon fiber paper with a gas diffusion layer on the air-facing side and a catalyst layer on the water-facing side was used as the air diffusion cathode, a polished Zn plate (0.3 mm in thickness, and 2 cm² in area) as the anode, and a solution of 0.2 M zinc acetate and 6.0 M KOH as the electrolyte. The catalyst ink was sprayed onto the carbon fiber paper at a mass loading of 2 mg cm⁻².

Solid-state Zn–air batteries were constructed by using a zinc foil (thickness 0.1 mm) as the anode, and a poly(vinyl alcohol) (PVA) gel polymer as the solid electrolyte. The PVA gel polymer was prepared by mixing 5.0 g of PVA powder with 50 mL of H₂O under continuous stirring at 90 °C until a transparent gel was obtained, followed by the addition of 5 mL of 6 M KOH and 0.2 M zinc acetate. After 30 min's stirring, the gel was transferred into a petri dish, cooled in a commercial freezer at –25 °C for 24 h, and then thawed at room temperature. Lastly, a shrinking tube with many holes was used as the package of the flexible

batteries.

2.5. Computational methods

DFT calculations were performed with the open-source planewave code, Quantum Espresso [26]. The generalized gradient approximation and projector augmented wave pseudopotentials with the exchange and correlation in the Perdew–Burke–Ernzerhof were used in all calculations, with the plane-wave cutoff energy fixed at 400 eV. The convergence of forces and energy on each atom during structural relaxation were set to 0.04 eV Å⁻¹ in force and 10⁻⁶ eV in energy, respectively. The Brillouin zone was sampled with a 3 × 2 × 1 Monkhorst-Pack k-point grid [27]. The vacuum space along the z-direction was more than 15 Å, large enough to avoid interplanar interactions. The unit cell of Ru was in the P-63/mmc symmetry group, whereas Pnnm for RuO₂. The heterogeneous interface model was constructed by Ru(100) and RuO₂(101) with a matching error less than 5%. For computing the hydrogen and OER adsorption energy, layer slab models of pure Ru, pure RuO₂, and Ru-RuO₂ heterojunction were constructed, respectively. For geometric optimization of all slab models, the top two layers were allowed to relax.

The computational hydrogen electrode was used to obtain adsorption energies for each state [28,29]. The four-electron OER pathway can be summarized by the following four elementary steps,



where the * stands for an active site on the catalyst surface, and l and g refer to liquid and gas phases, respectively, and *OH, *O and *OOH are adsorbed oxygenated intermediates.

The free energy of hydrogen adsorption on Ru(001), RuO₂(110), and Ru/RuO₂ hybrid nanostructure were calculated by using the following equations,

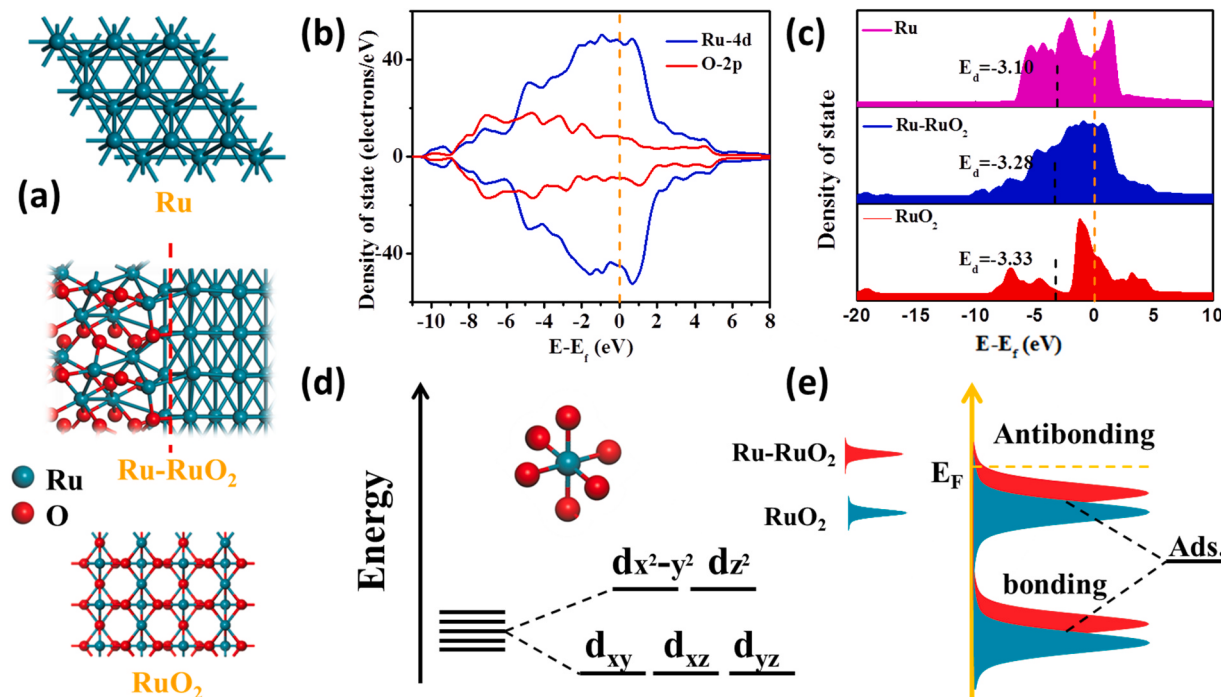


Fig. 1. (a) Schematic illustration of the atomic structure of Ru metal. (b) Density of states (DOS) of a Ru-RuO₂ heterojunction. (c) Projected DOS and d band of RuO₂ and Ru-RuO₂. (d) Orbital hybridization between Ru and Ru-O atoms. (e) Schematic of bond formation of adsorbates on catalyst surfaces.

$$\Delta G = \Delta E_{H*} + \Delta E_{ZPE} - T\Delta S \quad (5)$$

$$\Delta E_{H*} = E_{(surface+H*)} - (E_{H*} + E_{surface}) \quad (6)$$

where $E_{(surface+H*)}$ and $E_{surface}$ denote the energy of substrates with an adsorbed H atom and the energy of bare substrates, E_{H*} denotes half of the energy of H₂, ΔE_{ZPE} is the variation in zero-point energies and ΔS is the change in entropy before and after the reaction. T is temperature and equals to 298 K. Therefore, the free energy of the adsorbed state can be taken as $\Delta G = \Delta E_{H*} + 0.24\text{eV}$.

3. Results and discussion

3.1. Theoretical study of Ru-RuO₂ M-S heterojunctions

DFT calculations were first carried out to examine the impacts of the formation of Ru-RuO₂ M-S heterojunctions on the adsorption energy of important reaction intermediates. The Ru(100)/RuO₂(101) interface was used as the illustrating model (Fig. 1a). From the calculated density of states (DOS) (Fig. 1b), one can see that the heterostructure manifests metallic characters with a zero-band gap, and the Ru d-states are closer to the Fermi level (E_F), as compared to pristine RuO₂ (Fig. 1c). In fact, the d band center of the heterojunction (E_d = -3.28 V) can be seen to fall in the intermediate between those of metallic Ru (E_d = -3.10 V) and RuO₂ (-3.33 V) alone. As metallic Ru is the presumed active sites for HER [17], this suggests that the formation of a Ru-RuO₂ heterojunction leads to weakened adsorption of important reaction intermediates (e.g., H, and O) and may effectively enhance the catalytic activity, as compared to Ru metal alone.

The OER performance is likely to be enhanced as well, where RuO₂ has been recognized as an active component [19,30]. As orbital hybridization occurs between Ru and Ru-O at the interface, the d-band center is up-shifted (with a broadened d-band), as compared to RuO₂ alone (Fig. 1c). This can be understood by the unique coordination chemistry of the Ru centers within the framework of crystal field theory [31]. From Fig. 1d, one can see that the Ru in RuO₂ is coordinated to six

O atoms, forming an octahedral structure in D_{3h} symmetry; and the five 4d-orbitals of the Ru atom split into two groups, i.e., (d_{xy} , d_{xz} , d_{yz}) and ($d_{x^2-y^2}$, d_{z^2}). When intermediates adsorb onto the metal sites, the coupling between the adsorbate valence states and the Ru d orbitals leads to the splitting into bonding and antibonding states (Fig. 1e). The bonding states are typically completely filled as their energies are markedly lower than E_F , whereas the electron filling of the antibonding states, and hence the adsorption strength, depends on the energy relative to E_F .^[32] Since the antibonding states generally exhibit a higher energy than the d states, the d band center is a good descriptor of the adsorbate-metal interaction. The up-shift of the d band energy of the Ru-RuO₂ heterostructure, as compared to that of pristine RuO₂, indicates that the antibonding energy states rise and the interaction between adsorbates and hetero-interface is strengthened, a critical step towards enhanced OER.^[31]

Taken together, results from these DFT calculations show that the M-S heterojunction of Ru-RuO₂ leads to the formation of an appropriate d-band center that is conducive to both HER and OER electrocatalysis, as compared to pristine Ru and RuO₂. This is indeed confirmed by experimental measurements, as detailed below.

3.2. Sample preparation and structural characterization

The fabrication process of the Ru-RuO₂@NPC composites is schematically illustrated in Fig. 2. Experimentally, phytic acid and dicyandiamide were first cross-linked in solution, and the obtained compounds were coordinated with RuCl₃ and dispersed in a graphene oxide solution under stirring. The solution pH was adjusted to neutral ($pH \approx 7$) by the addition of NaHCO₃, prior to hydrothermal treatment at 150 °C for 6 h. XRD studies (Fig. S1) suggest that RuO₂ was generated during this process due to hydrolysis of part of the Ru³⁺ species. The products were then collected and subject to thermal annealing in an Ar atmosphere at 800 °C for 2 h, affording Ru-RuO₂@NPC. During this process, the continuous decomposition of dicyandiamide and phytic acid was accompanied by the release of nitrogen- and phosphorus-containing gases, leading to the generation of a porous carbon scaffold embedded with Ru-RuO₂ M-S nanoparticles.

When the pH of the precursor solution was increased to 9, the final product (RuO₂@NPC) contained only RuO₂ nanoparticles, but no metallic Ru, likely due to complete hydrolysis of Ru³⁺ into RuO₂. In contrast, when the precursor solution pH was decreased to 5 and thermal annealing was conducted in a mixed atmosphere of Ar (90%) and H₂ (10%), the obtained composite (Ru@NPC) contained only metallic Ru nanoparticles, but no RuO₂ (Fig. S1).

The structures of the Ru-RuO₂@NPC nanocomposites were first characterized by SEM measurements. From Fig. S2, the Ru-RuO₂@NPC nanocomposites can be seen to exhibit a sheet-like morphology composed of wrinkled graphene flakes (ca. 1.0 ~ 2.0 μm in length). In TEM measurements (Fig. 3a), one can see that the (low-contrast) graphene flakes were predominantly of few layers in thickness, contained

abundant mesopores and in-plane cavities, and were decorated with a number of (dark-contrast) nanoparticles that exhibited a diameter mostly in the range of 3–15 nm (Fig. 3a inset). In high-resolution TEM measurements (Figs. 3b, 3d and S3), the nanoparticles can be seen to consist of twin nanocrystals that are in intimate contact, both with clearly-defined lattice fringes but a slightly different electron density and interplanar spacing. The lighter part exhibited an interplanar spacing of 0.254 nm, corresponding to the (101) facets of RuO₂ (JCPDS no. 01-088-0323), whereas the darker one showed a spacing of 0.234 and 0.205 nm, in good agreement with the Ru(100) and (101) facets, respectively (JSPDS no. 06-0663). These results suggest the formation of Ru-RuO₂ M-S heterojunctions. Consistent results were obtained in selected area electron diffraction (SAED) measurements (Fig. 3c), where the (202) and (211) diffraction patterns of both Ru and RuO₂ can be clearly resolved.

Further structural insights were obtained in XRD measurements. From Fig. S4, the sample series (i.e., NPC, Ru@NPC, RuO₂@NPC, and Ru-RuO₂@NPC) can all be seen to display a broad peak centered at $2\theta = 25.5^\circ$, arising from the graphitic carbon (002) crystal planes. This is consistent with the lattice fringes in Fig. 3b inset that display a d-spacing of 0.350 nm, indicating successful formation of highly graphitized carbon.^[33] Ru@NPC displayed a series of additional diffraction peaks at $2\theta = 38.4^\circ, 42.2^\circ, 44.0^\circ, 58.3^\circ, 69.4^\circ, 78.3^\circ, 84.7^\circ$ and 85.9° that can be indexed to the (100), (002), (101), (102), (110), (103), (200), (112) and (201) planes of crystalline Ru (JSPDS no. 06-0663), respectively (Fig. S4b), whereas RuO₂@NPC featured peaks at $2\theta = 35.2^\circ, 54.9^\circ, 66.5^\circ$ and 74.2° (Fig. S4b) that are attributable to the (101), (121), (221) and (131) lattice planes of RuO₂ (JCPDS no. 01-088-0323), respectively. These patterns can all be seen with the Ru-RuO₂@NPC sample (Fig. S4a), consistent with the successful formation of Ru-RuO₂ M-S heterojunctions in the nanocomposites.

The elemental composition of the Ru-RuO₂@NPC sample was then evaluated by EDS-based mapping analysis, where the elements of Ru, P, N, O and C can be clearly identified (Fig. 3e). Notably, N, O and P exhibited a fairly even distribution throughout the sample (similar to NPC alone, Fig. S5), suggestive of homogeneous doping of these elements into the carbon matrix, whereas Ru was far more localized, coinciding with the isolated Ru-RuO₂ nanoparticles on the carbon nanosheet surface.

The coordination environment and electronic structure of the nanocomposites were then analyzed by X-ray absorption near-edge structure (XANES) and extended X-ray absorption fine structure (EXAFS) studies. From the normalized Ru K-edge XANES spectra in Fig. 4a, one can see that Ru-RuO₂@NPC, RuO₂ and Ru foil all displayed a similar absorption edge, white line, and post-edge oscillations, suggesting a rather consistent atomic structure and chemical states of the ruthenium atoms in the samples. However, from the zoom-in region of 22075 to 22150 eV (inset to Fig. 4a), it can be seen that the edge energy varies in the order of Ru foil < Ru-RuO₂@NPC < RuO₂, suggest that the average Ru valence state in Ru-RuO₂@NPC fell in between those of

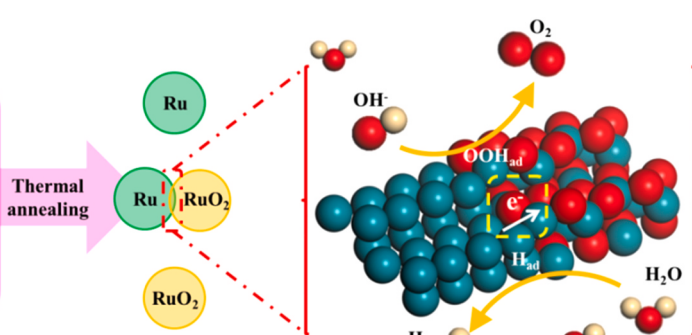
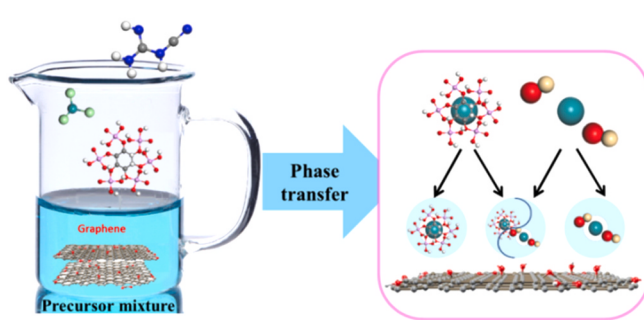


Fig. 2. Schematic depiction of the synthesis of Ru-RuO₂@NPC nanocomposites.

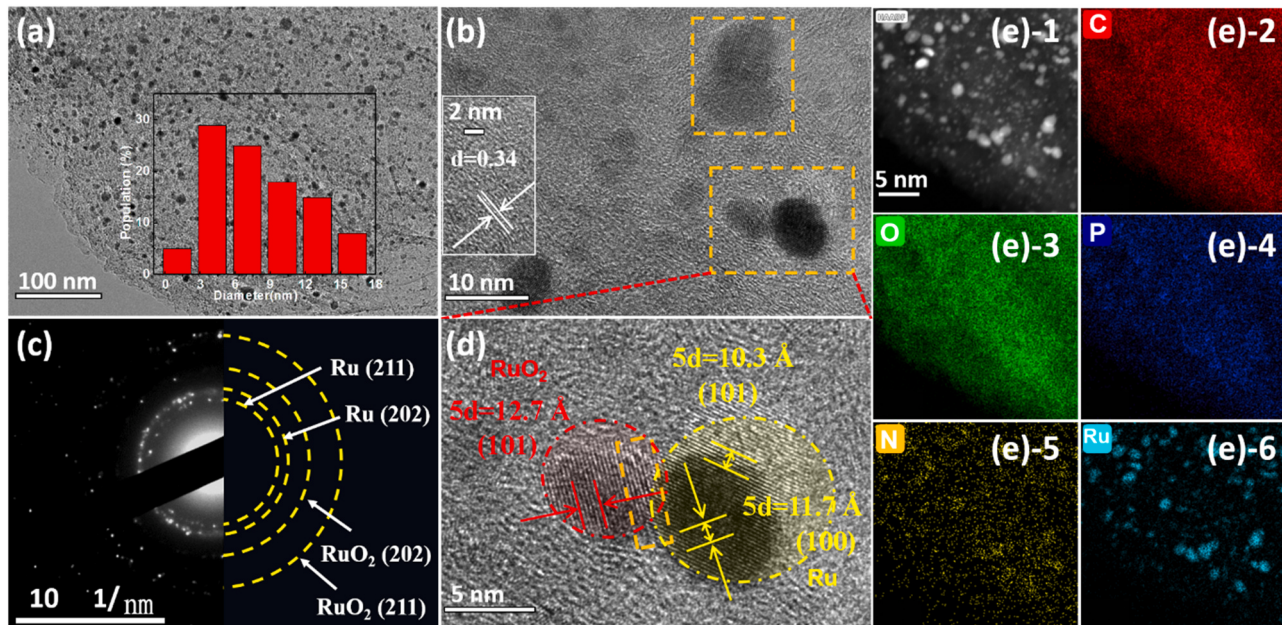


Fig. 3. (a, b) Representative TEM images and (c) SAED patterns of Ru-RuO₂@NPC. (d) High-resolution TEM image of the selected area in panel (b). (e-1) TEM image of Ru-RuO₂@NPC and the corresponding elemental maps of (e-2) C, (e-3) O, (e-4) P, (e-5) N, and (e-6) Ru. Inset to (a) is the corresponding core-size histogram of the Ru-RuO₂@NPC. Inset to (b) is a zoom in of the lattice fringes.

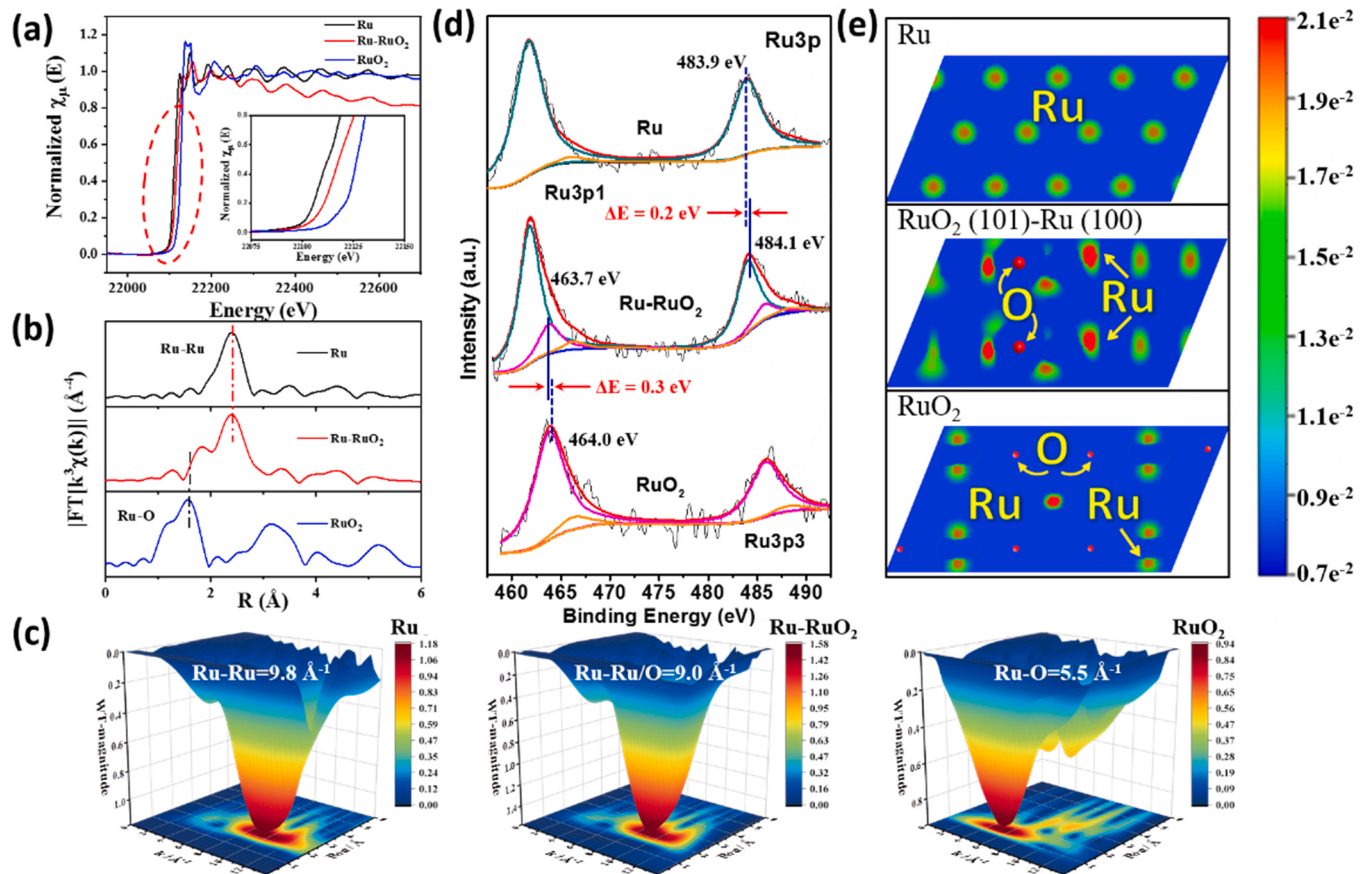


Fig. 4. (a) Ru K-edge XANES spectra and (b) Fourier transforms of the Ru K-edge EXAFS oscillations of Ru-RuO₂@NPC and reference samples (Ru foil and RuO₂). (c) WT-EXAFS of Ru foil, Ru-RuO₂@NPC and RuO₂. (d) High-resolution XPS spectra of the Ru 3p electrons in Ru@NPC, RuO₂@NPC and Ru-RuO₂@NPC, and (e) the corresponding surface charge density.

metallic Ru and RuO₂. The corresponding R space profiles via Fourier transforms (FTs) of the EXAFS spectra are displayed in Fig. 4b. One can see that the peak at 2.39 Å for Ru-Ru (Ru foil) and that at 1.57 Å for Ru-O (RuO₂) can both be identified with the Ru-RuO₂@NPC composite, suggesting a hybrid structure within the latter sample.

Consistent results were obtained in wavelet transform (WT) analysis. From Fig. 4c, both the Ru foil and RuO₂ can be seen to exhibit an intensity maximum in the WT contour plot, at 9.8 Å⁻¹ for the former (Ru-Ru coordination) and 5.5 Å⁻¹ for the latter (Ru-O coordination). By contrast, the intensity maximum of the Ru-RuO₂@NPC sample appeared at a somewhat different position of 9.0 Å⁻¹, in the intermediate between those of Ru and RuO₂, again, confirming the formation of a hybrid structure within the composite (which likely entails a major component of Ru and a minor one of RuO₂, as suggested in Fig. 3d and confirmed below).

The surface elemental composition and valence states of the nanocomposites were investigated by XPS measurements. As shown in Fig. S6, the C 1 s, O 1 s, N 1 s and P 2p peaks can be readily identified in the carbon scaffold (NPC), while in Ru-RuO₂@NPC, a clearly-defined Ru 3p peak appears at ca. 781.4 eV. Quantitative analysis of the integrated peak areas shows that the Ru-RuO₂@NPC nanocomposite consisted of 85.3 at% of C, 3.8 at% of N, 8.5 at% of O, 0.4 at% of P and 2.0 at% of Ru. This is in good agreement with results obtained from EDS measurements (Fig. S7), although the Ru content (2.0 at% or 14.2 wt%) was somewhat lower than that from ICP-OES measurements (17.2 wt%).

From the high-resolution scan of the Ru 3p electrons in Ru-RuO₂@NPC (Fig. 4d), two doublets can be deconvoluted, one at 461.9/484.1 eV and the other at 463.7/485.8 eV, due to the 2p_{3/2} and 2p_{1/2} electrons of Ru(0) and Ru(IV), respectively, in good agreement with the results presented above where the sample consisted of a Ru and RuO₂ hybrid [18,34–36]. Note that the binding energies of the Ru(0) doublet are ca. 0.2 eV higher than those of Ru@NPC, whereas the binding energies of the Ru(IV) doublet exhibit a negative shift of 0.3 eV, as compared to those of RuO₂@NPC. This suggests a reduced electron density of the metallic Ru component in Ru-RuO₂@NPC as compared to Ru@NPC, while the RuO₂ species in Ru-RuO₂@NPC was somewhat electron-richer than RuO₂@NPC, most probably as a result of the formation of an M-S heterojunction (Fig. 1 and 3) that led to effective interfacial charge transfer from Ru to RuO₂ [37]. In addition, from Fig. 4d, the contents of Ru and RuO₂ in the Ru-RuO₂@NPC hybrid were estimated to be ca. 1.62 and 0.38 at%, respectively, i.e., a Ru:RuO₂ molar ratio of ca. 4.3. Note that whereas H₂-TPR measurements suggested the existence of RuO₂ on the surface of Ru@NPC, the content was markedly lower than that on Ru-RuO₂@NPC (Fig. S8). This is likely the reason why it was not resolved in XPS measurements.

DFT calculations show a consistent variation of the surface charge density and density of states (Fig. 4e). On the pristine RuO₂ surface (bottom panel), the O atoms are electron-enriched because each surface Ru atom contributes ~4.0 electrons to its neighboring O atoms, according to Bader charge analysis. After the formation of a heterojunction with Ru metal (middle panel), the electron density of O is further increased, due to charge transfer from the electronegative Ru to the neighboring O and Ru⁴⁺ sites. Indeed, the Ru sites are obviously electron-deficient, as compared to the pristine Ru surface (top panel). Such interfacial interactions between Ru and RuO₂ in the M-S heterostructure are anticipated to impact the adsorption of important reaction intermediates and hence the electrocatalytic activities in various reactions (vide infra).

Fig. S9a shows the high-resolution scan of the Ru 3d and C 1 s electrons of the Ru-RuO₂@NPC composite, and data for other samples are shown in Fig. S10–S13. The doublet at 280.5/284.9 eV can be assigned to the Ru 3d_{3/2}/3d_{5/2} electrons [38,39]. The peak at 284.8 eV is attributed to sp²-hybridized C of graphene, while those at 286.2 and 288.4 eV are due to C-N/C-P/C-O and O-C=O, respectively [40]. The corresponding high-resolution scan of the N 1 s electrons is shown in Fig. S9b, where deconvolution yields four peaks at 398.6, 400.0, 401.4

and 403.9 eV, due to pyridinic N, pyrrolic N, graphitic N and oxidized N, respectively, indicating successful incorporation of N atoms into the carbon skeletons [41]. Similarly, from the P 2p spectrum in Fig. S9c, two sub-peaks can be resolved at 133.6 eV for P-O and 132.5 eV for P-C, suggesting the successful doping of P into the N-doped carbon framework. By contrast, no Ru-P peak is detected at about 130 eV, implying that P was not doped into the Ru nanoparticles during the synthetic process [42,43]. In the O 1 s spectrum (Fig. S9d), three peaks can be resolved at 531.2, 532.6 and 533.3 eV, and ascribed to C=O, C-O and O-H, respectively, whereas a fourth peak at 529.8 eV is attributed to lattice oxygen (O_{Lat}) from RuO₂ [44]. Note that the N and P contents (3.8 at% and 0.4 at%) in Ru-RuO₂@NPC were rather consistent with those (4.5 at% and 0.4 at%) of the metal-free NPC (Fig. S5f and S10, and Table S1).

The specific surface area and pore size distribution of the Ru-RuO₂@NPC nanocomposites were then evaluated by nitrogen adsorption/desorption measurements (Fig. S14). The Ru-RuO₂@NPC sample showed a type-IV N₂ adsorption–desorption isotherm, with a specific surface area of 212.0 m² g⁻¹, and pore diameters in the range of 2.0–40.0 nm, similar to those of NPC (258.0 m² g⁻¹). This indicates that the structure of the carbon scaffold remained essentially unchanged before and after the addition of Ru. The formation of the carbon skeletons was further confirmed by Raman spectroscopic measurements, where the D and G bands can be clearly observed in both NPC and Ru-RuO₂@NPC at ca. 1350 and 1578 cm⁻¹, respectively (Fig. S15). The ratio of the D and G band intensities (I_D/I_G) was also very close at 1.28 for NPC and 1.24 for Ru-RuO₂@NPC.

3.3. Trifunctional electrocatalytic activity

The HER and OER electrocatalytic activities of Ru-RuO₂@NPC were then examined by electrochemical measurements in a standard three-electrode configuration in electrolytes at widely different pH, 0.5 M H₂SO₄ (pH = 0), 1.0 M KOH (pH = 14) and 0.01 M PBS (pH = 7.5). We first investigated the OER activity in acidic media. From Fig. 5a, one can see that in comparison to the metal-free NPC, Ru@NPC and commercial RuO₂ exhibited only minimal activity, Ru-RuO₂@NPC and RuO₂@NPC were far more active, and Ru-RuO₂@NPC is obviously the best among the series. In fact, one can see that the Ru-RuO₂@NPC hybrid needed an overpotential ($\eta_{10,\text{OER}}$) of only 170 mV to reach the current density of 10 mA cm⁻², which is drastically lower than those of commercial RuO₂ (390 mV), RuO₂@NPC (260 mV), Ru@NPC (483 mV), and NPC (more than 600 mV) (Fig. 5a). To the best of our knowledge, the $\eta_{10,\text{OER}}$ of the Ru-RuO₂@NPC sample is the lowest in acidic media among relevant OER electrocatalysts reported so far (Table S2). The Ru-RuO₂@NPC nanocomposite also shows the best activity in alkaline ($\eta_{10,\text{OER}} = 190$ mV, Fig. 5b) and neutral ($\eta_{10,\text{OER}} = 440$ mV, Fig. 5c) media. These results are also summarized in Fig. 5d (left).

Moreover, Ru-RuO₂@NPC shows a Tafel slope of 47 mV dec⁻¹ in acidic media (Fig. S16a), which was much smaller than those of RuO₂@NPC (64 mV dec⁻¹), Ru@C (242 mV dec⁻¹), NPC (406 mV dec⁻¹), and commercial RuO₂ (269 mV dec⁻¹). A similar trend can be seen in alkaline media (Fig. S16b), suggesting favorable electron-transfer kinetics in these two electrolyte media. In neutral electrolyte, Ru-RuO₂@NPC also showed better kinetics than other samples (Fig. S16c). Consistent results were obtained in electrochemical impedance spectroscopy (EIS) measurements (Fig. S17), where Ru-RuO₂@NPC can be seen to display a smaller semicircle (charge-transfer resistance, R_{CT}) than commercial RuO₂ in all three electrolyte solutions.

Significantly, Ru-RuO₂@NPC also possessed high OER stability, as confirmed by chronoamperometric tests, where the current diminishment was markedly lower than that of commercial RuO₂ over a wide pH range of 0–14 (Fig. S18). This suggests enhanced stability of the heterostructured composites, as compared to the Ru or RuO₂ counterparts. Such an excellent OER performance may be due to the combined contributions of the electronic regulation of the M-S heterostructure in

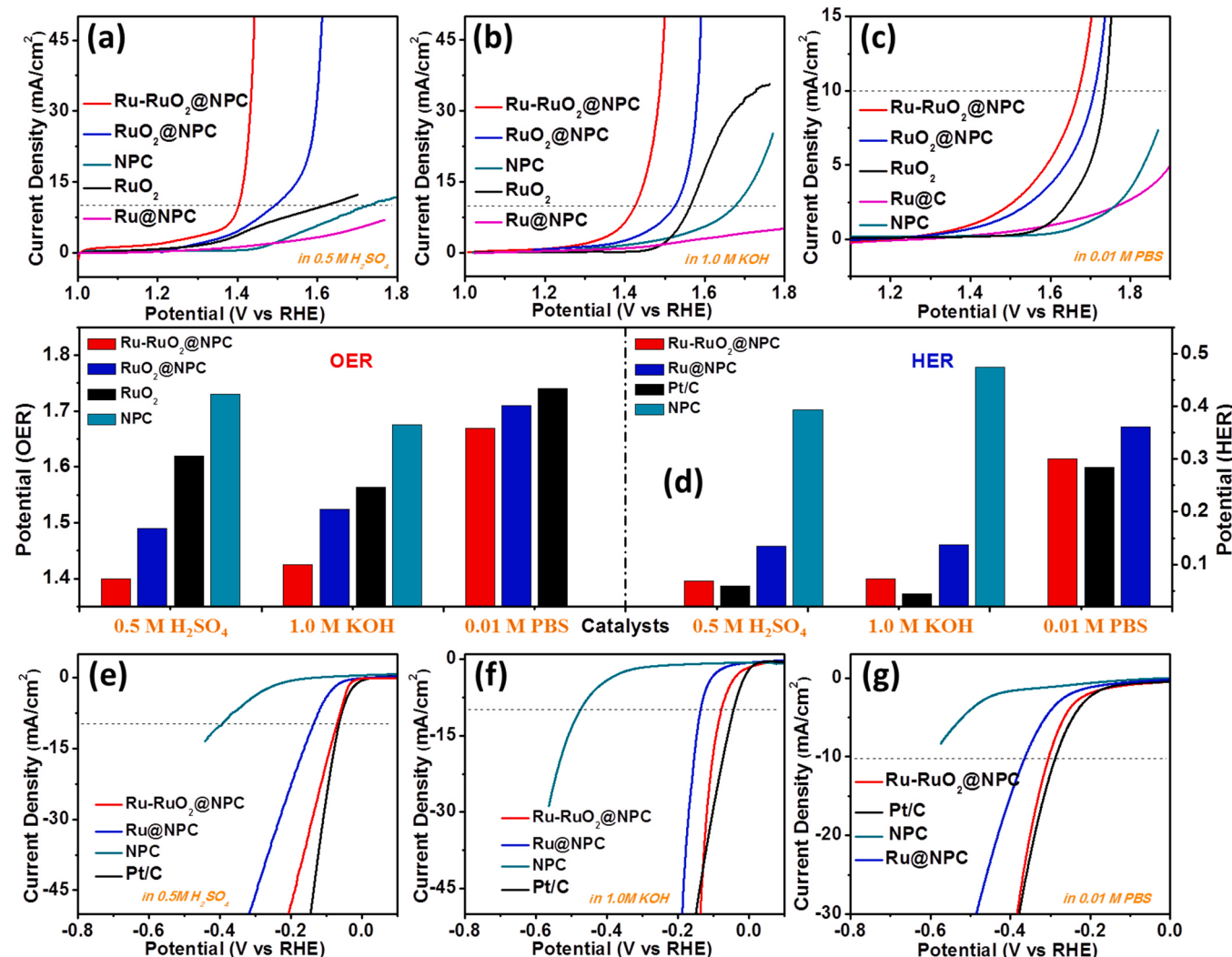


Fig. 5. Polarization curves of Ru-RuO₂@NPC, RuO₂@NPC, Ru@NPC, NPC, commercial RuO₂ and Pt/C for (a-c) OER and (e-g) HER in (a, e) 1.0 M KOH solution, (b, f) 0.5 M H_2SO_4 solution and (c, g) 0.01 M PBS solution after capacitance-correction and iR-correction at the potential sweeping rate of 10 mV s⁻¹. (d) Comparison of the required potentials at 10 mA cm^{-2} for the series of catalysts.

Ru-RuO₂ nanoparticles (Fig. 1), and the synergy between the hybrid nanoparticle and the carbon substrate.

Interestingly, Ru-RuO₂@NPC also shows significant electrocatalytic activity towards HER in the wide range of pH. In 0.5 M H_2SO_4 (pH = 0), Ru-RuO₂@NPC displayed a small onset potential of $\sim 23 \text{ mV}$ (vs. RHE, at the current density of 1 mA cm^{-2}) (Fig. 5e) and an overpotential ($\eta_{10, \text{HER}}$) of only $\sim 68 \text{ mV}$ at 10 mA cm^{-2} . The latter is only 10 mV more negative than that of Pt/C ($\sim 58 \text{ mV}$), but markedly better than those of Ru@NPC ($\sim 137 \text{ mV}$) and NPC ($\sim 395 \text{ mV}$), and among the lowest ever reported for HER by relevant catalysts (Table S2). This signifies the importance of Ru-RuO₂ M-S heterojunctions in boosting the HER electrocatalysis. Similar behaviors were observed in alkaline (Fig. 5f) and neutral media (Fig. 5g) [45,46].

Consistent results were obtained in Tafel analysis of the HER kinetics (Fig. S19), where Ru-RuO₂@NPC exhibited a Tafel slope of 56 mV dec^{-1} in acidic media (Fig. S19a), much smaller than that of Ru@NPC (113 mV dec^{-1}) and NPC (163 mV dec^{-1}), but larger than that of Pt/C (39 mV dec^{-1}) [47]. In 1.0 M KOH (Fig. S19b), the Ru-RuO₂@NPC sample shows a slightly higher Tafel slope of 73 mV dec^{-1} , indicating a similar reaction pathway. However, in neutral 0.01 M PBS (Fig. S19c), the Tafel slope is closed to 113 mV dec^{-1} , implying that HER was largely dictated by the Volmer reaction (discharge step).

The Ru-RuO₂@NPC nanocomposite also exhibited excellent stability

in HER electrocatalysis. As shown in Fig. S20, the HER polarization curve remained almost unchanged after 2000 cycles; and there is no apparent decay of the current at the fixed operating potential of $\sim 100 \text{ mV}$ for more than 10 h by chronoamperometric measurements in acidic, neutral and alkaline media, in comparison to Pt/C (Fig. S21). In fact, the sample structure remained largely unchanged, as attested by XRD, XPS and Raman measurements (Fig. S22). In contrast, apparent structural variations were observed with Ru@NPC and RuO₂@NPC after the long-term stability tests, (Fig. S23), where part of the Ru⁴⁺ on the RuO₂@NPC surface was found to be reduced to metallic Ru during HER, and there was a serious Ru dissolution from Ru@NPC during OER. In EIS measurements, the Ru-RuO₂@NPC nanocomposite also possesses a smaller R_{CT} than others in the series across this wide range of pH (Fig. S24). It is worth noting that the catalytic activity is even better than the results of most leading catalysts based on noble metals, non-noble metals and nonmetallic catalysts reported recently in the literature (Table S2).

In the above measurements, one can see that (i) the Ru-free NPC exhibited only negligible catalytic activities towards OER and HER, suggesting minimal contributions from heteroatom doping to the reactions; (ii) the HER catalytic performance was markedly improved by the addition of Ru, whereas the addition of RuO₂ led to enhanced OER activity; and (iii) Ru-RuO₂@NPC served as effective bifunctional

electrocatalysts, displaying the highest activity towards both HER and OER among the series, suggesting the unique contributions of the Ru-RuO₂ M-S heterojunctions to the electrocatalytic performance.

This is indeed confirmed by results from DFT calculations, where the formation of Ru-RuO₂ M-S heterojunctions led to a clear variation of the E_d value. Specifically, DFT studies were conducted to evaluate the electronic structure of the Ru(100)/RuO₂(101) interface and the fundamental implication in the catalytic activity towards HER and OER. The Ru-RuO₂ twin particles observed experimentally (Fig. 3) were modeled as an M-S heterojunction on a carbon surface (Fig. S25). Note that OER is a four-electron process including the formation of *OH, *O, *OOH, and O₂ intermediates, and the surface Ru centers of the heterojunction most likely acted as the adsorption sites of these oxygenated species [48–50]. Fig. 6a shows the atomic structures of oxygen intermediates adsorbed onto the Ru(100)/RuO₂(101) interface during the OER process; and the corresponding energy landscapes of the reaction

steps on Ru, RuO₂ and Ru-RuO₂ heterostructure are calculated and depicted in Fig. 6c. The advantages of the heterostructure can be clearly observed. Note that the adsorption energy difference between the *OOH and *O intermediates, which is the third elementary step (from *O to *OOH), is a key descriptor of OER activity [11,51,52]. One can see that the formation of *OOH on Ru-RuO₂ heterostructure exhibited a relatively low energy barrier of 1.78 eV, as compared to 2.76 eV on pristine RuO₂. Interestingly, although the energy barrier of step II on Ru was smaller than on RuO₂, the large energy barrier in the formation of *OH and *OOH (2.76 eV) suggested that the reaction was energetically impeded. That is, the Ru-RuO₂ heterostructure is anticipated to exhibit a higher electrocatalytic activity, because of the optimized electronic structures and lower reaction energy barrier.

For HER, the reaction in alkaline or neutral media involves a two-step pathway, i.e., adsorption and dissociation of a H₂O molecule, and adsorption of H from the catalyst surfaces (Fig. 6b) [16]. First-principles

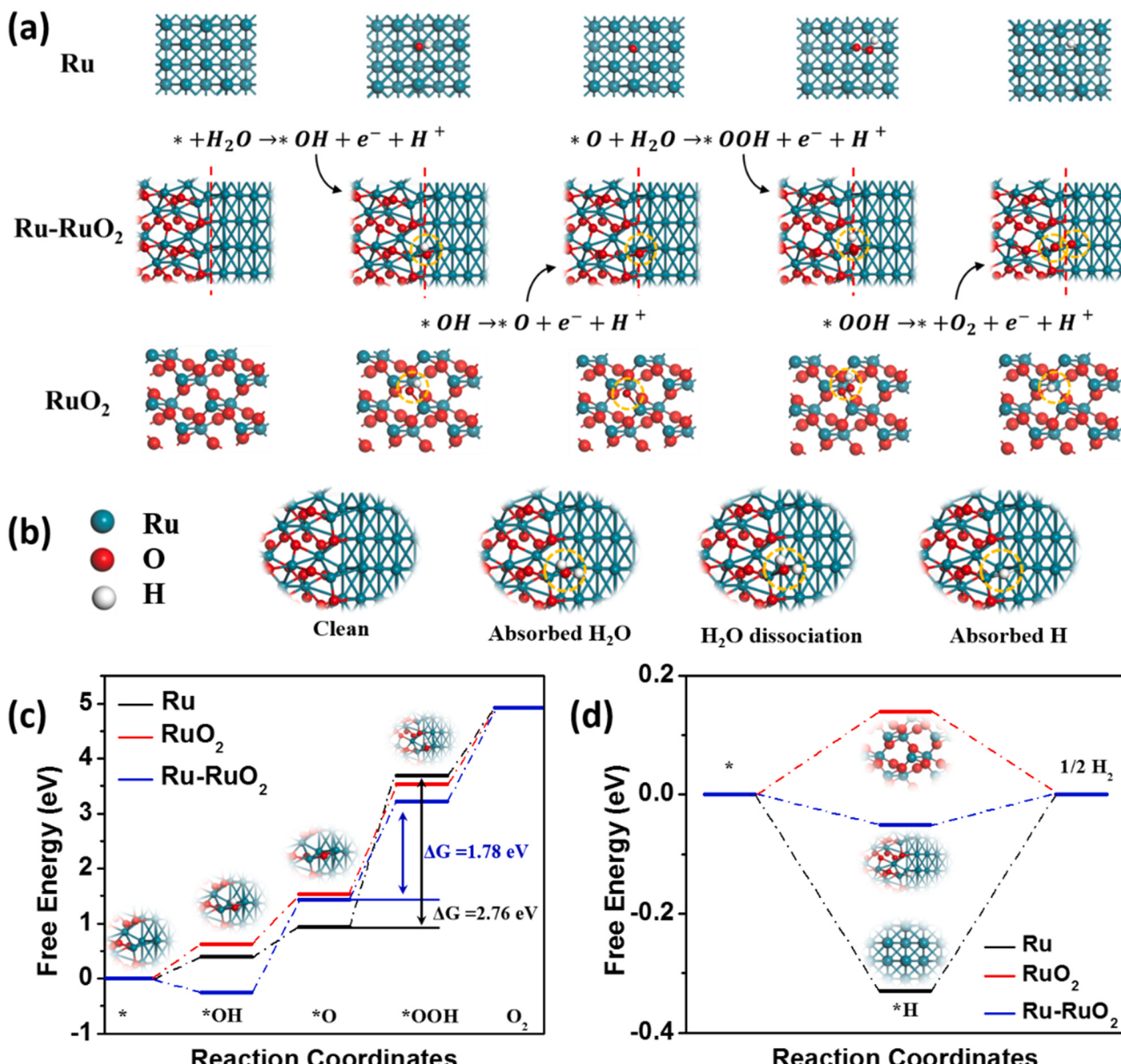


Fig. 6. DFT simulations for understanding the optimized catalytic mechanism over Ru(100), RuO₂(101) and Ru(100)/RuO₂(101) interface. (a) Schematic illustration of the atomic structures of intermediate adsorption during OER process, (b) Atomic configurations of the water dissociation step on the surface of the Ru-RuO₂ Mott-Schottky-Type heterostructure, including H₂O adsorption, activated H₂O adsorption, OH adsorption and H adsorption, (c) Free energy diagrams for OER and (d) energetic pathway of HER.

calculations showed that the Gibbs free energy (ΔG_{H^+}) on pristine Ru and RuO₂ lattices was relatively high, at -0.33 eV on Ru and 0.12 eV on RuO₂, but decreased drastically to only -0.05 eV on the Ru-RuO₂ heterojunction (Fig. 6d), consistent with the markedly improved HER performance observed experimentally [52]. This also indicates that the formation of Ru-RuO₂ M-S heterojunction was conducive to the adsorption/desorption of H [43]. Theoretically, the OER and HER activity of N and P doped carbon has been widely reported, due to manipulation of the density of electronic states and formation of catalytic active sites [42]. Yet in the present study, the Ru-RuO₂ heterostructures made dominant contributions to the HER/OER activity, as manifested above.

With the remarkable catalytic activity towards both OER and HER, the Ru-RuO₂@NPC composite was then tested as a bifunctional catalyst for electrochemical water splitting. Fig. 7a shows the current profiles acquired in 1.0 M KOH with Ru-RuO₂@NPC serving as both the cathode and anode catalysts (Fig. 7a). From Fig. 7b, it can be seen that the current increased sharply when the cell bias was past 1.30 V, producing a large number of bubbles on the electrode surface (inset to Fig. 7b). This indicates that Ru-RuO₂@NPC could indeed effectively catalyze overall water splitting. Specifically, a low cell bias of 1.46 V was needed to

reach the current density of 10 mA cm⁻² in 1.0 M KOH, corresponding to a combined overpotential (at both anode and cathode) of only 230 mV for full water splitting. This is markedly lower than that (1.58 V) based on a mixture of commercial Pt/C-RuO₂. As shown in Fig. 7c and inset, the hydrogen and oxygen gases collected show a molar ratio of approximately $2:1$, according to the volume-time curve.

The Ru-RuO₂@NPC also exhibited significant electrocatalytic activity towards ORR in an oxygen-saturated 0.1 M KOH solution (Figs. S26 and S27). The outstanding bifunctional performance of Ru-RuO₂@NPC towards ORR/OER was further evidenced by overall oxygen electrode curves (Fig. S28), where the activity was evaluated by the difference between the OER potential at 10 mA cm⁻² and the ORR half-wave potential ($\Delta E = E_{OER,10} - E_{ORR,1/2}$). When the catalyst is used as a reversible oxygen electrode, a smaller ΔE represents a lower efficiency loss and a better activity [53]. Clearly, the Ru-RuO₂@NPC shows the smallest ΔE of 0.65 V (0.1 M KOH) and 0.56 V (1.0 M KOH) among the series of catalysts under study. What is more, such a ΔE value of 0.65 V is also the smallest, to the best of our knowledge, as compared to relevant trifunctional catalysts for ORR and OER reported recently in the literature (Table S3).

These results suggest that the nanocomposites might also be used as

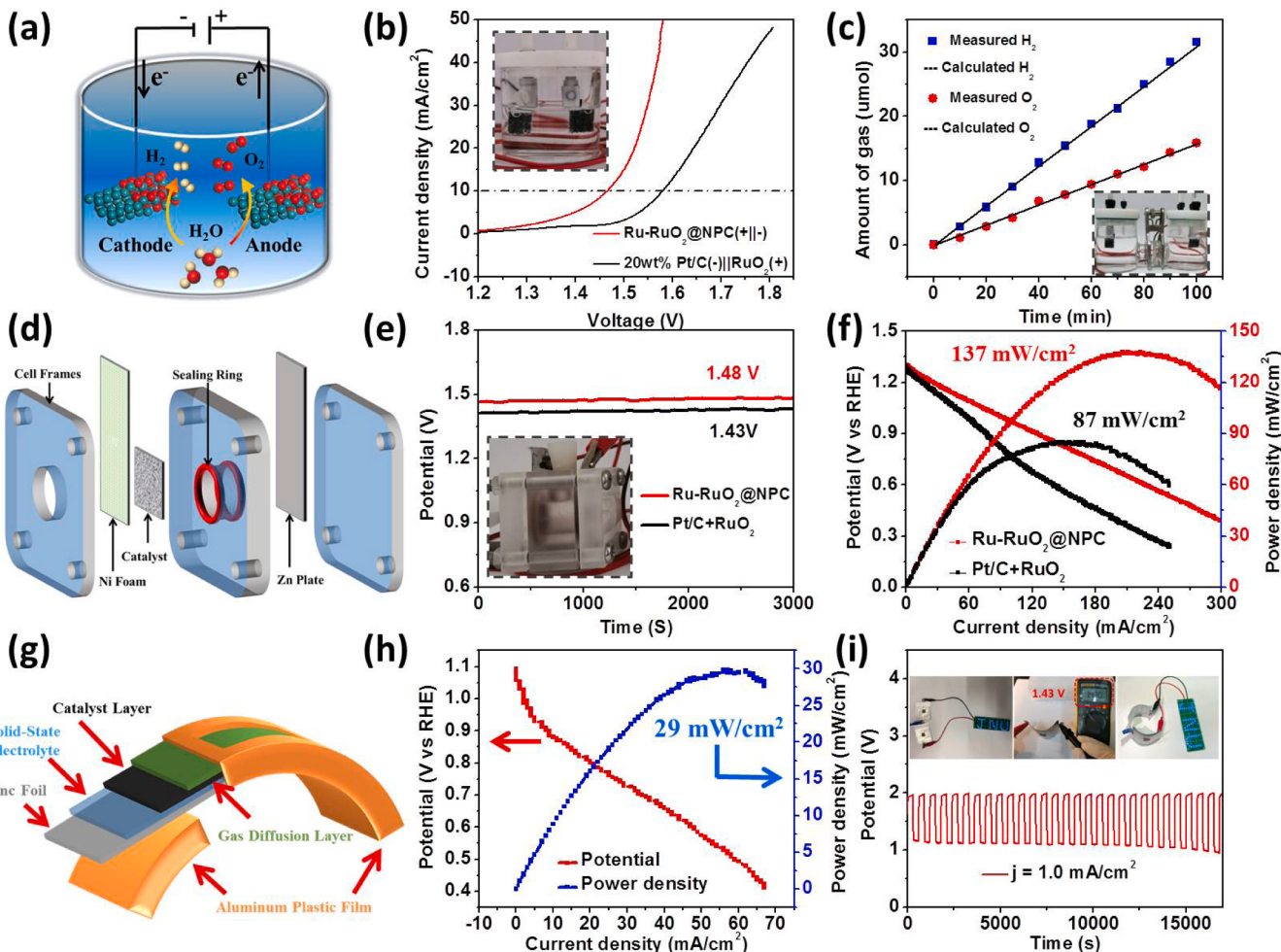


Fig. 7. (a) Schematic illustration of water splitting cell. (b) LSV curves of the Ru-RuO₂@NPC in 1.0 M KOH in a two-electrode system. Inset shows the digital photograph of H₂ and O₂ bubbles evolving from the electrodes during electrolysis. (c) Comparison between the theoretical and experimental yields of the O₂ and H₂ gases produced from Ru-RuO₂@NPC water splitting under a constant current of 1.0 mA. Inset shows the L-shaped electrolytic cell used to collect gases during the reaction. (d) Schematic diagram of an aqueous zinc-air battery. (e) Open-circuit potential and (f) discharging polarization curves and corresponding power plots of a home-made Zn-air battery (panel (e) inset). (g) Schematic diagram of a flexible solid-state rechargeable Zn-air battery, and the corresponding (h) polarization and power density curves, and (i) charge and discharge voltage profiles with Ru-RuO₂@NPC being the bifunctional oxygen electrocatalyst. Inset to panel (i) shows the photographs of the battery with an open circuit voltage of 1.43 V (middle photo), and two flexible solid-state Zn-air batteries connected in series to light up a blue LED screen at the bending angle of 0° (left photo) and 90° (right photo), respectively.

the oxygen catalysts for reversible metal-air batteries. This was indeed manifested with zinc-air batteries using the Ru-RuO₂@NPC as a free-standing flexible air cathode (Fig. 7d–f and Fig. S29), and the corresponding zinc-air battery can be used as a power source to drive water splitting (Fig. S30). To demonstrate the potential applications in wearable devices, we also constructed a solid-state flexible battery with potassium hydroxide/polyvinyl alcohol gel as the electrolyte (Fig. 7g). The battery exhibited an open circuit voltage of 1.43 V (Fig. 7i middle inset) and a high-power density of 29 mW cm⁻². Notably, only two batteries connected in series were needed to light a blue LED screen (Fig. 7i left inset), and no impact on the device performance was observed even when the batteries were bent at 90° (Fig. 7i right inset).

4. Conclusions

Motivated by results from DFT calculations, Ru-RuO₂@NPC nanocomposites were prepared by a facile pyrolysis process where Ru-RuO₂ M-S heterojunctions were formed and supported on N,P-codoped carbon. Remarkably, the Ru-RuO₂@NPC hybrids was found to exhibit a remarkable activity towards HER, ORR, and OER within a wide range of solution pH and could be used as a high-performance, bifunctional catalyst for overall water splitting and oxygen electrocatalysts for rechargeable metal-air batteries. The significantly enhanced performance was attributed to the strong electronic interaction between Ru and RuO₂ in the heterostructures and the up-shift of the Ru d and O p band centers, which facilitated the adsorption/desorption of critical intermediates in the various reactions. Results from this study highlight the significance of M-S heterojunctions in the manipulation of the electronic properties of catalytic active sites and hence the ensuing electron-transfer dynamics in electrochemical reactions. Such mechanistic insights will be of fundamental significance in the design and engineering of high-performance catalysts for electrochemical energy technologies.

CRediT authorship contribution statement

N. W. carried out the majority of the work and drafted the paper. S. N. conducted the DFT calculations. X. Y., D. C., Z. L., J. X., and D. Z. assisted in data acquisition and analysis. Q.L. and B.L. assisted in data analysis and paper editing. H. M. and L. L. led the team at JNU and SCUT, respectively, and edited the paper. S. W. C. led the effort at UCSC and finalized the draft.

Declaration of Competing Interest

The authors declare that they have no known competing financial interests or personal relationships that could have appeared to influence the work reported in this paper.

Acknowledgment

This work was supported by the National Natural Science Foundation of China (22075102); the Natural Science Foundation of Guangdong Province, China (2017A030313048); the Fundamental Research Funds for the Central Universities (21620329) and the Postdoctoral Research Foundation of China (2020M673071). S.W.C. thanks the US National Science Foundation for partial support of the work (CHE-1900235 and CHE-2003685).

Appendix A. Supporting information

Supplementary data associated with this article can be found in the online version at [doi:10.1016/j.apcatb.2021.120838](https://doi.org/10.1016/j.apcatb.2021.120838).

References

- [1] J. Liu, Z. Wang, J. Li, L. Cao, Z. Lu, D. Zhu, Structure engineering of MoS₂ via simultaneous oxygen and phosphorus incorporation for improved hydrogen evolution, *Small* 16 (2020), 1905738, <https://doi.org/10.1002/smll.201905738>.
- [2] J.A. Turner, Sustainable hydrogen production, *Science* 305 (2004) 972–974, <https://doi.org/10.1126/science.1103197>.
- [3] Z.W. Seh, J. Kibsgaard, C.F. Dickens, I. Chorkendorff, J.K. Nørskov, T.F. Jaramillo, Combining theory and experiment in electrocatalysis: Insights into materials design, *Science* 355 (2017) eaad4998, <https://doi.org/10.1126/science.aad4998>.
- [4] B. Tang, J. Yang, Z. Kou, L. Xu, H.L. Seng, Y. Xie, A.D. Handoko, X. Liu, Z.W. Seh, H. Kawai, Surface-engineered cobalt oxide nanowires as multifunctional electrocatalysts for efficient Zn-Air batteries-driven overall water splitting, *Energy Storage Mater.* 23 (2019) 1–7, <https://doi.org/10.1016/j.ensm.2019.05.046>.
- [5] K.R.G. Lim, A.D. Handoko, S.K. Nemanic, B. Wyatt, H.-Y. Jiang, J. Tang, B. Anasori, Z.W. Seh, Rational design of two-dimensional transition metal carbide/nitride (MXene) hybrids and nanocomposites for catalytic energy storage and conversion, *ACS nano* 14 (2020) 10834–10864, <https://doi.org/10.1021/acsnano.0c05482>.
- [6] N.-T. Suen, S.-F. Hung, Q. Quan, N. Zhang, Y.-J. Xu, H.M. Chen, Electrocatalysis for the oxygen evolution reaction: recent development and future perspectives, *Chem. Soc. Rev.* 46 (2017) 337–365, <https://doi.org/10.1039/C6CS00328A>.
- [7] L.C. Seitz, C.F. Dickens, K. Nishio, Y. Hikita, J. Montoya, A. Doyle, C. Kirk, A. Vojvodic, H.Y. Hwang, J.K. Nørskov, A highly active and stable IrO_x/SrIrO₃ catalyst for the oxygen evolution reaction, *Science* 353 (2016) 1011–1014, <https://doi.org/10.1126/science.aaf5050>.
- [8] J.N. Tiwari, S. Sultan, C.W. Myung, T. Yoon, N. Li, M. Ha, A.M. Harzandi, H. J. Park, D.Y. Kim, S.S. Chandrasekaran, Multicomponent electrocatalyst with ultralow Pt loading and high hydrogen evolution activity, *Nat. Energy* 3 (2018) 773–782, <https://doi.org/10.1038/s41560-018-0209-x>.
- [9] J. Di, C. Yan, A.D. Handoko, Z.W. Seh, H. Li, Z. Liu, Ultrathin two-dimensional materials for photo- and electrocatalytic hydrogen evolution, *Mater. Today* 21 (2018) 749–770, <https://doi.org/10.1016/j.mattod.2018.01.034>.
- [10] H. Sun, Y. Lian, C. Yang, L. Xiong, P. Qi, Q. Mu, X. Zhao, J. Guo, Z. Deng, Y. Peng, A hierarchical nickel–carbon structure templated by metal–organic frameworks for efficient overall water splitting, *Energy Environ. Sci.* 11 (2018) 2363–2371, <https://doi.org/10.1039/C8EE00934A>.
- [11] G. Zhou, M. Li, Y. Li, H. Dong, D. Sun, X. Liu, L. Xu, Z. Tian, Y. Tang, Regulating the electronic structure of CoP nanosheets by O incorporation for high-efficiency electrochemical overall water splitting, *Adv. Funct. Mater.* 30 (2020), 1905252, <https://doi.org/10.1002/adfm.201905252>.
- [12] X.K. Wan, H.B. Wu, B.Y. Guan, D. Luan, X.W. Lou, Confining sub-nanometer Pt clusters in hollow mesoporous carbon spheres for boosting hydrogen evolution activity, *Adv. Mater.* 32 (2020), 1901349, <https://doi.org/10.1002/adma.201901349>.
- [13] M. Aleksandrzak, W. Kukulka, E. Mijowska, Graphitic carbon nitride/graphene oxide/reduced graphene oxide nanocomposites for photoluminescence and photocatalysis, *Appl. Surf. Sci.* 398 (2017) 56–62, <https://doi.org/10.1016/j.apsusc.2016.12.023>.
- [14] M.P. Browne, Z. Sofer, M. Pumera, Layered and two dimensional metal oxides for electrochemical energy conversion, *Energy Environ. Sci.* 12 (2019) 41–58, <https://doi.org/10.1039/C8EE02495B>.
- [15] B.H. Suryanto, Y. Wang, R.K. Hocking, W. Adamson, C. Zhao, Overall electrochemical splitting of water at the heterogeneous interface of nickel and iron oxide, *Nat. Commun.* 10 (2019) 1–10, <https://doi.org/10.1038/s41467-019-13415-8>.
- [16] Q. Wu, M. Luo, J. Han, W. Peng, Y. Zhao, D. Chen, M. Peng, J. Liu, F.M. de Groot, Y. Tan, Identifying electrocatalytic sites of the nanoporous copper–ruthenium alloy for hydrogen evolution reaction in alkaline electrolyte, *ACS Energy Lett.* 5 (2019) 192–199, <https://doi.org/10.1021/acsenergylett.9b02374>.
- [17] Q. Yao, B. Huang, N. Zhang, M. Sun, Q. Shao, X. Huang, Channel-rich RuCu nanosheets for pH-universal overall water splitting electrocatalysis, *Angew. Chem., Int. Ed.* 58 (2019) 13983–13988, <https://doi.org/10.1002/ange.201908092>.
- [18] J. Yu, Y. Guo, S. She, S. Miao, M. Ni, W. Zhou, M. Liu, Z. Shao, Bigger is surprisingly better: agglomerates of larger RuP nanoparticles outperform benchmark Pt nanocatalysts for the hydrogen evolution reaction, *Adv. Mater.* 30 (2018), 1800047, <https://doi.org/10.1002/adma.201800047>.
- [19] J. Liu, Y. Zheng, Y. Jiao, Z. Wang, Z. Lu, A. Vasileff, S.Z. Qiao, NiO as a bifunctional promoter for RuO₂ toward superior overall water splitting, *Small* 14 (2018), 1704073, <https://doi.org/10.1002/smll.201704073>.
- [20] J. Hou, Y. Sun, Y. Wu, S. Cao, L. Sun, Promoting active sites in core–shell nanowire array as Mott–Schottky electrocatalysts for efficient and stable overall water splitting, *Adv. Funct. Mater.* 28 (2018), 1704447, <https://doi.org/10.1002/adfm.201704447>.
- [21] D. Liang, C. Lian, Q. Xu, M. Liu, H. Liu, H. Jiang, C. Li, Interfacial charge polarization in Co₂P₂O₇@N, P co-doped carbon nanocages as Mott–Schottky electrocatalysts for accelerating oxygen evolution reaction, *Appl. Catal., B* 268 (2020), 118417, <https://doi.org/10.1016/j.apcatb.2019.118417>.
- [22] Z.H. Xue, H. Su, Q.Y. Yu, B. Zhang, H.H. Wang, X.H. Li, J.S. Chen, Janus Co/CoP nanoparticles as efficient Mott–Schottky electrocatalysts for overall water splitting in wide pH range, *Adv. Energy Mater.* 7 (2017), 1602355, <https://doi.org/10.1002/aenm.201602355>.
- [23] Z. Sun, Y. Wang, L. Zhang, H. Wu, Y. Jin, Y. Li, Y. Shi, T. Zhu, H. Mao, J. Liu, Simultaneously realizing rapid electron transfer and mass transport in jellyfish-like Mott–Schottky nanoreactors for oxygen reduction reaction, *Adv. Funct. Mater.* 30 (2020), 1910482, <https://doi.org/10.1002/adfm.201910482>.

[24] Y. He, Q. He, L. Wang, C. Zhu, P. Golani, A.D. Handoko, X. Yu, C. Gao, M. Ding, X. Wang, Self-gating in semiconductor electrocatalysis, *Nat. Mater.* 18 (2019) 1098–1104, <https://doi.org/10.1038/s41563-019-0426-0>.

[25] R. Kou, Y. Shao, D. Mei, Z. Nie, D. Wang, C. Wang, V.V. Viswanathan, S. Park, I. A. Aksay, Y. Lin, Y. Wang, J. Liu, Stabilization of electrocatalytic metal nanoparticles at metal–metal oxide–graphene triple junction points, *J. Am. Chem. Soc.* 133 (2011) 2541–2547, <https://doi.org/10.1021/ja107719u>.

[26] P. Giannozzi, S. Baroni, N. Bonini, M. Calandra, R. Car, C. Cavazzoni, D. Ceresoli, G.L. Chiarotti, M. Cococcioni, I. Dabo, QUANTUM ESPRESSO: a modular and open-source software project for quantum simulations of materials, *J. Phys.: Condens. Matter* 21 (2009), 395502, <https://doi.org/10.1088/0953-8984/21/39/395502>.

[27] N. Marzari, D. Vanderbilt, A. De Vita, M. Payne, Thermal contraction and disordering of the Al (110) surface, *Phys. Rev. Lett.* 82 (1999) 3296–3299, <https://doi.org/10.1103/PhysRevLett.82.3296>.

[28] J. Zhang, Z. Zhao, Z. Xia, L. Dai, A metal-free bifunctional electrocatalyst for oxygen reduction and oxygen evolution reactions, *Nat. Nanotechnol.* 10 (2015) 444–452, <https://doi.org/10.1038/NNANO.2015.48>.

[29] Y. Zheng, Y. Jiao, Y. Zhu, Q. Cai, A. Vasileff, L.H. Li, Y. Han, Y. Chen, S.-Z. Qiao, Molecule-level $g\text{-C}_3\text{N}_4$ coordinated transition metals as a new class of electrocatalysts for oxygen electrode reactions, *J. Am. Chem. Soc.* 139 (2017) 3336–3339, <https://doi.org/10.1021/jacs.6b13100>.

[30] K.A. Stoerzinger, O. Diaz-Morales, M. Kolb, R.R. Rao, R. Frydendal, L. Qiao, X. R. Wang, N.B. Halck, J. Rossmeisl, H.A. Hansen, Orientation-dependent oxygen evolution on RuO_2 without lattice exchange, *ACS Energy Lett.* 2 (2017) 876–881, <https://doi.org/10.1021/acsenergylett.7b00135>.

[31] S. Sun, X. Zhou, B. Cong, W. Hong, G. Chen, Tailoring the d-band centers endows $(\text{Ni} \times \text{Fe}1-\text{x})_2\text{P}$ nanosheets with efficient oxygen evolution catalysis, *ACS Catal.* 10 (2020) 9086–9097, <https://doi.org/10.1021/acscatal.0c01273>.

[32] Z. Chen, Y. Song, J. Cai, X. Zheng, D. Han, Y. Wu, Y. Zang, S. Niu, Y. Liu, J. Zhu, Tailoring the d-band centers enables Co_4N nanosheets to be highly active for hydrogen evolution catalysis, *Angew. Chem.* 130 (2018) 5170–5174, <https://doi.org/10.1002/ange.201801834>.

[33] H. Kabir, H. Zhu, J. May, K. Hamal, Y. Kan, T. Williams, E. Echeverria, D. N. McIlroy, D. Estrada, P.H. Davis, The $\text{sp}^2\text{-sp}^3$ carbon hybridization content of nanocrystalline graphite from pyrolyzed vegetable oil, comparison of electrochemistry and physical properties with other carbon forms and allotropes, *Carbon* 144 (2019) 831–840, <https://doi.org/10.1016/j.carbon.2018.12.058>.

[34] S.J. Choi, J.S. Jang, H.J. Park, I.D. Kim, Optically sintered 2D RuO_2 nanosheets: temperature-controlled NO_2 reaction, *Adv. Funct. Mater.* 27 (2017), 1606026, <https://doi.org/10.1002/adfm.201606026>.

[35] A.A. Jelle, K.K. Ghuman, P.G. O'Brien, M. Hmadeh, A. Sandhel, D.D. Perovic, C. V. Singh, C.A. Mims, G.A. Ozin, Solar fuels: highly efficient ambient temperature CO_2 photomethanation catalyzed by nanostructured RuO_2 on silicon photonic crystal support (Adv. Energy Mater. 9/2018), *Adv. Energy Mater.* 8 (2018), 1870041, <https://doi.org/10.1002/aenm.201870041>.

[36] J. Hu, T. Qu, Y. Liu, X. Dai, Q. Tan, Y. Chen, S. Guo, Y. Liu, Core–shell-structured CNT@ hydroxyl RuO_2 as a H_2/CO_2 fuel cell cathode catalyst to promote CO_2 methanation and generate electricity, *J. Mater. Chem. A* 9 (2021) 7617–7624, <https://doi.org/10.1039/D0TA11232A>.

[37] H. Liuyong, X. Zeng, X. Wei, H. Wang, W. Yu, G. Wenling, S. Le, C. Zhu, Interface engineering for enhancing electrocatalytic oxygen evolution of NiFe LDH/NiTe heterostructures, *Appl. Catal., B* (2020), 119014, <https://doi.org/10.1016/j.apcatb.2020.119014>.

[38] K.-H. Kwak, D.W. Kim, Y. Kang, J. Suk, Hierarchical Ru-and RuO_2 -foams as high performance electrocatalysts for rechargeable lithium–oxygen batteries, *J. Mater. Chem. A* 4 (2016) 16356–16367, <https://doi.org/10.1039/C6TA05077H>.

[39] D.J. Morgan, Resolving ruthenium: XPS studies of common ruthenium materials, *Surf. Interface Anal.* 47 (2015) 1072–1079, <https://doi.org/10.1002/sia.5852>.

[40] Z. Lin, G. Waller, Y. Liu, M. Liu, C.P. Wong, Facile synthesis of nitrogen-doped graphene via pyrolysis of graphene oxide and urea, and its electrocatalytic activity toward the oxygen-reduction reaction, *Adv. Energy Mater.* 2 (2012) 884–888, <https://doi.org/10.1002/aenm.201200038>.

[41] H.B. Yang, J. Miao, S.-F. Hung, J. Chen, H.B. Tao, X. Wang, L. Zhang, R. Chen, J. Gao, H.M. Chen, Identification of catalytic sites for oxygen reduction and oxygen evolution in N-doped graphene materials: development of highly efficient metal-free bifunctional electrocatalyst, *Sci. Adv.* 2 (2016), e1501122, <https://doi.org/10.1126/sciadv.1501122>.

[42] J. Zhang, L. Qu, G. Shi, J. Liu, J. Chen, L. Dai, N, P-codoped carbon networks as efficient metal-free bifunctional catalysts for oxygen reduction and hydrogen evolution reactions, *Angew. Chem.* 128 (2016) 2270–2274, <https://doi.org/10.1002/ange.201510495>.

[43] Z. Pu, I.S. Amiuu, Z. Kou, W. Li, S. Mu, RuP₂-based catalysts with platinum-like activity and higher durability for the hydrogen evolution reaction at all pH values, *Angew. Chem., Int. Ed.* 56 (2017) 11559–11564, <https://doi.org/10.1002/anie.201704911>.

[44] Y. Song, X. Zhang, Y. Zhou, Q. Jiang, F. Guan, H. Lv, G. Wang, X. Bao, Promoting oxygen evolution reaction by RuO_2 nanoparticles in solid oxide CO_2 electrolyzer, *Energy Storage Mater.* 13 (2018) 207–214, <https://doi.org/10.1016/j.ensm.2018.01.013>.

[45] Z.-F. Huang, J. Song, K. Li, M. Tahir, Y.-T. Wang, L. Pan, L. Wang, X. Zhang, J.-J. Zou, Hollow cobalt-based bimetallic sulfide polyhedra for efficient all-pH-value electrochemical and photocatalytic hydrogen evolution, *J. Am. Chem. Soc.* 138 (2016) 1359–1365, <https://doi.org/10.1021/jacs.5b11986>.

[46] J. Staszak-Jirkovský, C.D. Malliakas, P.P. Lopes, N. Danilovic, S.S. Kota, K.-C. Chang, B. Genorio, D. Strmcnik, V.R. Stamenkovic, M.G. Kanatzidis, Design of active and stable Co–Mo–Sx chalcogels as pH-universal catalysts for the hydrogen evolution reaction, *Nat. Mater.* 15 (2016) 197–203, <https://doi.org/10.1038/NMAT4481>.

[47] Z. Zhuang, J. Huang, Y. Li, L. Zhou, L. Mai, The holy grail in platinum-free electrocatalytic hydrogen evolution: molybdenum-based catalysts and recent advances, *ChemElectroChem* 6 (2019) 3570–3589, <https://doi.org/10.1002/celc.201900143>.

[48] Z. Zhao, H. Liu, W. Gao, W. Xue, Z. Liu, J. Huang, X. Pan, Y. Huang, Surface-engineered PtNi–O nanostructure with record-high performance for electrocatalytic hydrogen evolution reaction, *J. Am. Chem. Soc.* 140 (2018) 9046–9050, <https://doi.org/10.1021/jacs.8b04770>.

[49] H. Han, K.M. Kim, H. Choi, G. Ali, K.Y. Chung, Y.-R. Hong, J. Choi, J. Kwon, S. W. Lee, J.W. Lee, Parallelized reaction pathway and stronger internal band bending by partial oxidation of metal sulfide–graphene composites: important factors of synergistic oxygen evolution reaction enhancement, *ACS Catal.* 8 (2018) 4091–4102, <https://doi.org/10.1021/acscatal.8b00017>.

[50] H. Fei, J. Dong, Y. Feng, C.S. Allen, C. Wan, B. Voloskiy, M. Li, Z. Zhao, Y. Wang, H. Sun, General synthesis and definitive structural identification of Mn_4C_4 single-atom catalysts with tunable electrocatalytic activities, *Nat. Catal.* 1 (2018) 63–72, <https://doi.org/10.1038/s41929-017-0008-y>.

[51] Z. Zhuang, Y. Wang, C.-Q. Xu, S. Liu, C. Chen, Q. Peng, Z. Zhuang, H. Xiao, Y. Pan, S. Lu, Three-dimensional open nano-netcage electrocatalysts for efficient pH-universal overall water splitting, *Nat. Commun.* 10 (2019) 1–10, <https://doi.org/10.1038/s41467-019-12885-0>.

[52] Y. Liu, S. Liu, Y. Wang, Q. Zhang, L. Gu, S. Zhao, D. Xu, Y. Li, J. Bao, Z. Dai, Ru modulation effects in the synthesis of unique rod-like $\text{Ni}@\text{Ni}_2\text{P}$ –Ru heterostructures and their remarkable electrocatalytic hydrogen evolution performance, *J. Am. Chem. Soc.* 140 (2018) 2731–2734, <https://doi.org/10.1021/jacs.7b12615>.

[53] Y. Zhao, K. Kamiya, K. Hashimoto, S. Nakanishi, Efficient bifunctional Fe/C/N electrocatalysts for oxygen reduction and evolution reaction, *J. Phys. Chem. C* 119 (2015) 2583–2588, <https://doi.org/10.1021/jp511515q>.